Indian Journal of Chemical Technology
Vol. 29, March 2022, pp. 128-138

Z-scheme heterojunction of Bi_2S_3/g-C_3N_4 and its photocatalytic effect

Yachu Meng[1], Yuzhen Li*[,1], Yunsheng Xia[2] & Wenjun Chen[3]

[1]College of Environmental Science and Engineering, Taiyuan University of Technology, Taiyuan, 030024, China
[2]Department of Chemistry, Bohai University, Jinzhou 121 013, China
[3]Shanxi Provincial People,s Hospital, Taiyuan 030012, China

Received 5 November 2021; accepted 3 February 2022

In this study, Bi_2S_3/g-C_3N_4 binary catalyst has been excellently prepared by a wet impregnation-calcination method to form Z-scheme heterojunction. The catalyst has been characterized by X-ray diffraction (XRD), transmission electron microscopy (TEM), ultraviolet-visible diffuse reflectance spectroscopy (UV-DRS) and photoluminescence spectroscopy (PL). The physicochemical properties of the catalyst have been tested, such as crystal structure, morphology, optical properities, light absorption properties and luminescence properties. The results demonstrate that the photocatalytic activity is significantly increased when Bi_2S_3 with optimum weight percentage (5wt%) loaded into g-C_3N_4. Through photocatalytic degradation experiments, the optimal loading ratio, dosage and dye concentration of binary materials have been explored. At the same time, the effect of *p*H on the photocatalytic experiment under the optimal conditions is studied. Reactive blue 19 (RB19) is degraded by 97.77% in 2 h as the target pollutants. The trapping experiment further verified that $\cdot O_2^-$ is the main active species in photocatalytic degradation of RB19.

Keywords: Bi_2S_3/g-C_3N_4, Photocatalysis, Wet impregnation calcination method, Z-scheme

Nowadays, the problems on environmental deterioration and energy shortage have been bothering people, and green chemistry has become a necessary requirement for the sustainable development of human society[1].With the development of industrialization and urbanization, environmental pollution and energy crisis are two urgent problems that seriously threaten human health and ecological environment[1]. The increasing global crisis of energy shortage and environmental issues pose a serious threat to the long-term development of human society[2]. In particular, 0.7 million tons of organic synthetic dyes are approximately produced annual year around the global[3]. The organic dyes mainly come from bleaching industry, medicine manufacturing, and paper manufacturing. The dyes add colour to the water, preventing the solar light from reaching a deeper level of water, and reducing the photosynthesis of the plants in the aquatic ecosystem[4]. The main issue concerns the negative impact of synthetic dyes on the environment. It not only inhibits photosynthesis and consumes dissolved oxygen in water, but also has certain toxicity to animals, plants and humans. For example, if the synthetic dyes such as azo dyes degraded anaerobically, the generated aromatic amines were very toxic, carcinogenic and mutant[5]. Therefore, the direct release of colored wastewater into the aquatic ecosystems has escalated various threatening deterioration towards food chain interference and public health.

In order to solve these problems, there are many researchers using multiple methods to purify printing and dyeing waste water. The common methods of waste water treatment are adsorption, Fenton, oxidation, electrolysis and biological treatment[6]. These methods have distinct shortcomings, such as high cost, long treatment cycle and poor treatment efficiency.

Photocatalysis is an environmentally acceptable treatment technique in which pollutants are degraded by visible light. This method is considered to be effective to solve the problem of environmental pollution under the current energy deficiency[7]. It is found that photocatalysis has the advantages of low cost, environmental friendliness and wide application. It is driven by sustainable green solar energy, which is considered one of the most effective ways to address environmental problems[8]. In 1972, Fujishima proposed a semiconductor photocatalytic technology by using the discovery of photocatalytic decomposition of aquatic hydrogen with titanium dioxide electrode[9]. In 1997, Wang *et al.* reported on the amphiphilicity of titanium dioxide thin films at Nature, and made a great breakthrough in the application research[10]. Generally,

TiO_2 has been the benchmark of photocatalysts because of its wide availability and high performance. It has been widely used for organic dye decomposition, water splitting, and CO_2 reduction[11,12]. However, the band gap value of titanium dioxide was 3.2 eV, therefore there were two main issues of low solar energy conversion rate and high photogenerated electron-hole pair recombination rate[13].

Among many photocatalysts, the heptazine-based polymer melon (widely known as g-C_3N_4) with unique structure has become a research hotspot in recent years[14-16]. Graphite phase carbon nitride was a kind of non-metallic polymer with semiconductor-like properties. Its structural unit was a heptazine ring (C_6N_7) structure composed of C and N elements through sp_2 hybridization. It was connected by terminal N atoms and expands indefinitely to form a planar large-pi bond structure. These planar structures were then stacked into graphite-like layer structure. G-C_3N_4 has been widely used in photocatalytic fields, such as visible light hydrolysis degradation of organic pollutants[17]. Matthew et al. synthesized iron oxide doped carbon nitride in 3D printed and LED driven photon concentrator[18]. Li *et al.* fabricated novel rugby-like g-C_3N_4/$BiVO_4$ core/shell Z-scheme composites via low-temperature hydrothermal method to enhance photocatalytic performance[19]. Furthermore, Liu *et al*. prepared porous defective g-C_3N_4 ultrathin nanosheets through thermal condensation of freeze-dried precursor[20]. Although C_3N_4[21] was an excellent photocatalytic material, there were still many shortcomings on its development[22], such as low quantum efficiency, low visible light photoelectric conversion rate, low specific surface area, limited active sites and difficult recovery. In order to overcome these problems, many methods have been studied to improve the photocatalytic performance of g-C_3N_4. It mainly included reduction of grain size, doping of transition metal ions, deposition of noble metal surface, doping of non-metal ions, surface photosensitization, semiconductor composite and preparation of mesoporous photocatalysis. Heterogeneous nanocomposites based on g-C_3N_4 were prepared[23].

Especially, bismuth sulfide (Bi_2S_3), a superb photoconductive semi-conductor with a direct band gap (1.3-1.7eV), has been considered as promising material due to its cost-effective, non-poisonous nature, high mechanical and chemical stability, and easy synthesis for commercial applications[24]. Furthermore, it was a non-toxic and layered semiconductor material interconnected by weak Bi-S bonds. Due to outstanding electrical properties, it has been attracted much attention and has widely used in various fields such as thermoelectric, solar cells, photocatalysis, resistance switching and optical switching[25]. Hu *et al.* covered the one-pot synthesis of step-scheme Bi_2S_3/porous g-C_3N_4 heterostructure for enhanced photocatalytic performance[1]. Guo *et al.* synthesized Bi_2S_3 quantum dots (QDs)/g-C_3N_4 composites with various Bi_2S_3 QDs contents by hydrothermal method and used in CO_2 photocatalytic reduction[26]. Liu *et al*. studied 3D flower-like Bi_2S_3/BiOCl heterostructures to facilitate the separation of photogenerated electron-hole pairs and the production of active species about $\cdot O_2^-$ and h^{+}[27].

In order to improve the photocatalytic activity of g-C_3N_4, Bi_2S_3 was used to modify g-C_3N_4 to form Z-scheme heterojunction. Reactive blue (RB19) was used as the target pollutant to evaluate its photocatalytic activity. The effects of catalyst dosage, initial concentration of RB19 solution and *p*H on the catalytic performance were also studied. Finally, it was found that the active species were used to explain the photocatalytic process and the mechanism of photocatalytic degradation was deduced from the experimental results.

Experimental Section

Materials

All chemicals were analytical grade and used without further purification. Urea (H_2NCONH_2, 99%) was purchased from Tianjin Damao chemical reagents factory. $Bi(NO_3)_3 \cdot 5H_2O$ (99%) was purchased from Tianjin Kaitong Chemical Reagent Co., Ltd. KI (99%) and Reactive RB19 were purchased from Tianjin Guangfu Technology Development Co., Ltd. Ethylene glycol was purchased from Tianjin Jinfeng Chemical Co., Ltd. Methanol and ammonium oxalate (AO) (99.5%) were purchased from Tianjin Zhiyuan Chemical Reagent Co., Ltd. Benzoquinone (BQ) (99%) was purchased from Tianjin Qinghua Jinying Technology Co., Ltd. Tert-butyl alcohol (TBA) was purchased from Tianjin Beichen Founder Reagent Factory. Distilled water was used in the experimental processes.

Preparation of catalysts

Preparation of g-C_3N_4

Urea of 10.5 g and melamine of 4.5 g were weighed and placed in alumina crucible and heatedto 550°C for 4 h at the rate of 5°C/min. Yellow g-$C_3N_4$was obtained which was then grounded into powder. The powder sample g-C_3N_4 was obtained by

grinding and recycling after the reaction cooling to room temperature.

Synthesis of Bi_2S_3

The prepared $Na_2S_2O_3·5H_2O$ (0.7445g) and $Bi(NO_3)_3·5H_2O$ (1.9403g) were weighed and added with 50 mL methanol, then ultrasounded for 10 min and stirred for 60 min. The solution was transferred to a Teflon stainless-steel autoclave and heated at 180°C for 12 h. Bi_2S_3 was washed with distilled water andethanol several times and dried at 60°C.

Synthesis of g-C_3N_4/Bi_2S_3 heterojunction

Initially, 1 g of g-C_3N_4 was dissolved in 80 mL methanol and ultrasounded for 30 min to obtain solution A. Then added different quality Bi_2S_3 and ultrasounded for 60 min to obtain solution B, which stirred for 24 h and dried at 60°C. Finally calcined at 250°C for 3 h. Binary catalysts were recorded as 3BCS (0.03 g), 5BCS (0.05 g), 10BCS (0.10 g), 15BCS (0.15 g) and 20BCS (0.20 g) according to the mass doping ratio of Bi_2S_3, respectively.

Characterization

The X-ray diffraction data was measured by powder X-ray diffractometer (XRD, LABXRD-6000, Japan) with Cu Kα source (λ = 0.154 nm) at accelerating voltage and current of 40 kV and40 mA, respectively. UV-Vis diffuse reflectance spectroscopy (UV-DRS) was performed on a Shimadzu UV-2450 spectrophotometer with $BaSO_4$ as a reference. The structure and morphology of samples were observed on a field emission transmission electron microscope (JEM-2500SE, Japan). The photocatalytic photoluminescence spectrum was recorded in the wavelength range of 400-700 nm on a Shimadzu RF-6000 fluorescence spectrophotometer (PL, Japan) with an excitation wavelength of 380 nm.

Photocatalytic performance evaluation

The photocatalytic activities of the samples were conducted for the photo-degradation of the RB19. The reaction light source was a 300 W xenon lamp with 420 nm cut filter. Its working voltage was 14 V and its working current was 15 A. The binary catalyst of 0.2000 g was dissolved in RB19 solution with a concentration of 250 mL and 25 mg/L. And the ultrasound was dispersed for 10 min. The dark reaction lasted for 40 min. After reaching the adsorption and desorption equilibrium, the light source was turned on for the light reaction. The photoreaction lasted 120 min. Samples of 10 mL were taken every 20 min and centrifuged at 10,000 rpm for two more centrifugations every 5 min to ensure complete separation of the catalyst. The maximum absorption wavelength of RB19 was 594 nm.

The photocatalytic efficiency (η) of RB19 was computed according to the following formula:

$$\eta = \frac{C}{C_0} \quad \ldots(1)$$

Where: C_0 was the initial concentration of the dye, and Cwas the concentration of RB19 after time t.

The following formula was used to compute the first order rate constant (K_{obs}) of Bi_2S_3/g-C_3N_4 (Ref.28):

$$K_{obs} = -\frac{1}{t}\ln(\frac{C}{C_0}) \quad \ldots(2)$$

in which, C and C_0 are concentrations of RB19 in time of t and zero, respectively.

In addition to exploring the optimum loading ratio of Bi_2S_3/g-C_3N_4, the effects of catalyst dosage, initial RB19 concentration and initial pH on the performance of the catalyst were also studied. Free radical trapping experiments were carried out to explore the photocatalytic performance.

Effect of loading ratio of Bi_2S_3 on photocatalytic performance

RB19 25 mg/L was used to test the influence of the amount of Bi_2S_3 loaded in g-C_3N_4 on the degradation of RB19 as the target pollutant. The mass ratios of Bi_2S_3 added were 3wt%, 5wt%, 10wt%, 15wt% and 20wt%, respectively. Under the same experimental conditions, it was compared that the effects of different Bi_2S_3 loaded Bi_2S_3/g-C_3N_4 on the degradation of RB19.

Figure 1 showed the photocatalytic activity graphs of g-C_3N_4, Bi_2S_3, *x*BCS (*x*= 3, 5, 10, 15 and 20 wt% with *x* representing the weight percentages of Bi_2S_3). It could be seen from the Fig.1a that the adsorption capacity of g-C_3N_4 was relatively large, about 31.36%, the degradation capacity of Bi_2S_3 was 11.41%. With the increase of Bi_2S_3 loading amount, the dark adsorption capacity of Bi_2S_3/g-C_3N_4 to RB19 decreased first and then increased. Adsorption was lowest when the loading amount reached 10%. When Bi_2S_3 was doped into g-C_3N_4 from 3% to 10%, the dark adsorption capacity of the catalyst decreased from 24.46% to 16.94%, while from 10% to 20%, the dark adsorption capacity increased from 16.94% to

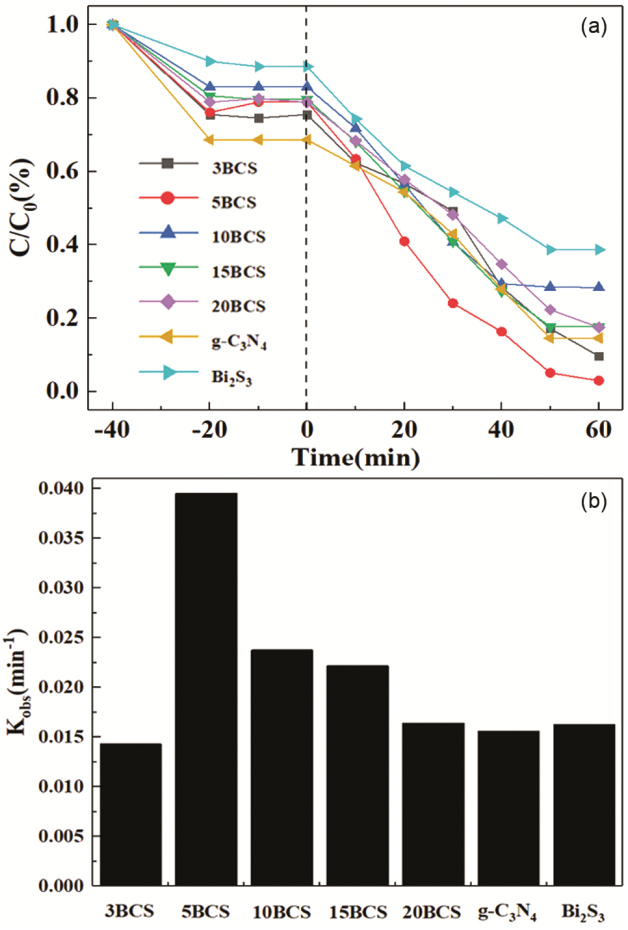

Fig. 1 — (a) Photocatalytic activities of different photocatalysts based on the photodegradation of RB19 under visible light and (b) Photodegradation rate constant (K_{obs}) of RB19 degradation in different samples.

21.10%, respectively. After 120 min photoreaction, g-C_3N_4 could degrade RB19 to about 85.43%, Bi_2S_3 to only 80.95%, while the final degradation of 5BCS could reach 96.99%.

As can be seen from the Fig. 1(b). As the interaction between g-C_3N_4 and Bi_2S_3 increased, so does the K_{obs} between them. With the increase of Bi_2S_3 doping, the first order rate constant of Bi_2S_3/g-C_3N_4 increased first and then decreased. When the mass ratio of Bi_2S_3 reached 5%, the first order rate constant of Bi_2S_3/g-C_3N_4 degradation of RB19 reached its peak. The K_{obs} of g-C_3N_4, Bi_2S_3,3BCS, 5BCS, 10BCS, 15BCS and 20BCS were 0.78×10^{-2}, 0.813×10^{-2}, 1.430×10^{-2}, 3.954×10^{-2}, 2.376×10^{-2}, 2.219×10^{-2} and 1.642×10^{-2} min^{-1},respectively. The K_{obs} of 5BCS was the largest. In a word, considering adsorption capacity, degradation capacity and the first order rate constant of Bi_2S_3/g-C_3N_4 degradation of

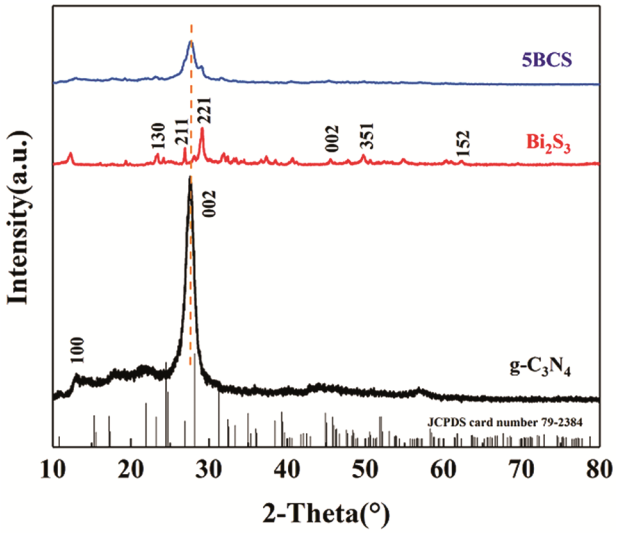

Fig. 2 — XRD patterns of pure g-C_3N_4, bare Bi_2S_3 and binary 5BCS.

RB19, we chased the 5BCS as the best loading-catalyst for subsequent experiments.

Results and Discussion

XRD analysis

The XRD patterns were performed to explore the crystal texture and composition of the obtained samples. Figure 2 show that the XRD patterns of g-C_3N_4, Bi_2S_3 and 5BCS. Two distinct diffraction peaks at 13.02° and 27.52° can be found for g-C_3N_4, which corresponded to the (100) and (002) planes of hexagonal g-C_3N_4(JCPDS 87-1526)[Ref.29]. The results were the same as in the previous study. There were obvious characteristic peaks of Bi_2S_3[Ref.30], the characteristic diffraction peaks located at2θ = 23.44°, 29.1°, 31.94°, 45.56°, 52.46°, 62.40° could be attributed to the planes (130), (211), (221), (002), (351), (152) of orthorhombic phase of Bi_2S_3 (JCPDS 17-0320)[Ref. .31-32]. Over the XRD pattern of 5BCS, we found all the diffraction peaks corresponding to g-C_3N_4 and Bi_2S_3, and did not find other peaks. This suggested that the two materials were well doped together and the high purity of the as-prepared samples. Meanwhile, we could significantly see that the peaks of the doped material decreased at each diffraction plane, the weakening of the peaks might be due to the agglomerate of Bi_2S_3 (Ref. 33).

TEM analysis

The morphology and micro structure of the catalyst were investigated by TEM. It could be seen from Fig. 3(a), (b) and(c). It showed that g-C_3N_4 was a

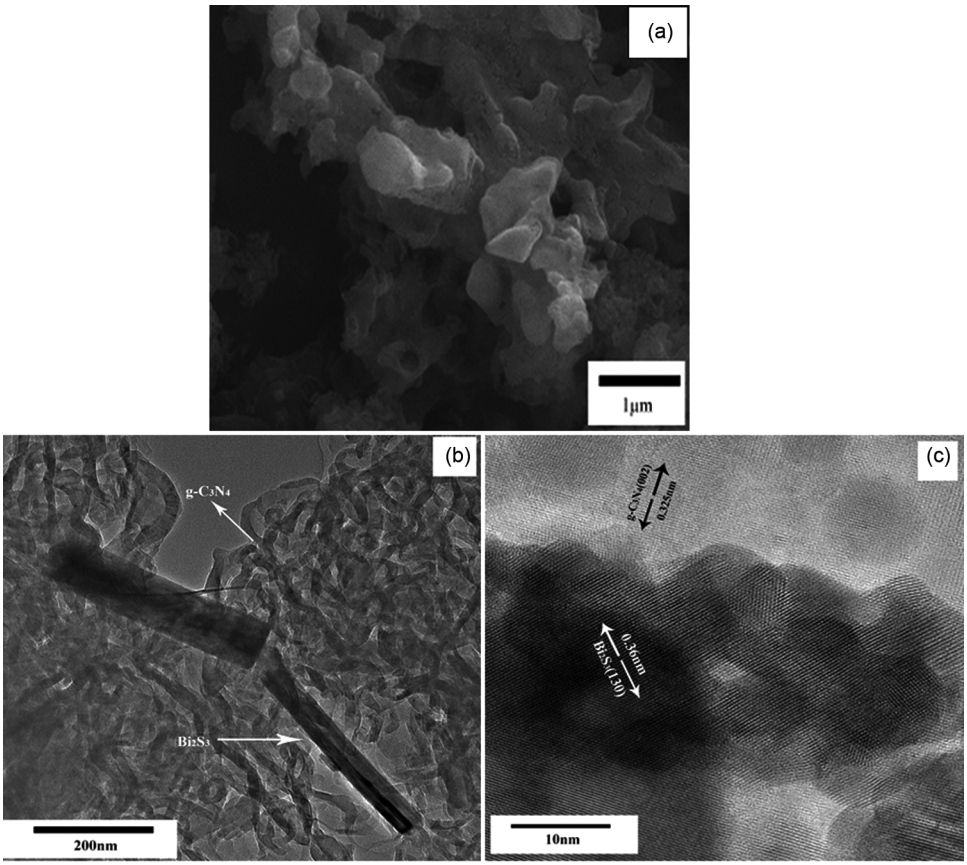

Fig. 3 — (a) TEM images of bare g-C_3N_4, (b) Binary 5BCS composites and (c) HR-TEM images of bare 5BCSscale bar 10 nm.

multilayer sheet structure from Fig. 3(a), which increased the specific surface area of catalyst and increase the adsorption capacity. It showed obviously from Fig. 3(b) that Bi_2S_3 was a bar bismuth structure and it was well combined on g-C_3N_4. The TEM [Fig. 3(c)] further demonstrated that the lattice fringes with interlayer spacing were0.360 nm and 0.325 nm, corresponding to the (130) plane of Bi_2S_3 and (002) plane of g-C_3N_4, respectively[34-36]. Based on the above, it further showed that Bi_2S_3 was well attached to g-C_3N_4. The result explained the successful construction of composite photocatalyst.

UV-Vis DRS analysis

The optical properties of Bi_2S_3/g-C_3N_4 photocatalyst, as well as bare Bi_2S_3 and g-C_3N_4 were analyzed using UV-Vis DRS technique, and the results were shown in Fig. 4. Obviously, the result showed that the samples had different absorption of pure g-C_3N_4, Bi_2S_3 and 5BCS in the range of 400-800 nm. The absorption was obvious in the visible region. As depicted in Fig. 4(a), the optical absorption edge of pure g-C_3N_4 and Bi_2S_3 were about 465 nm and 1130 nm, respectively[37,38], which was consistent with previous studies. It was obvious that the absorption edge of 5BCS was between g-C_3N_4 and Bi_2S_3, which was about 485 nm. Absorption in visible light range increased significantly and showed a red shift compared with pure g-C_3N_4. It displayed that the preparation of 5BCS can preferably improve the optical absorption property and increase the utilized efficiency of solar light, which was favourable for the enhancement of the photocatalytic activity[39].

As displayed in Fig. 4(b), the band gap values of the catalysts were approximately 2.74, 1.68 and2.25 eV for g-C_3N_4, Bi_2S_3 and 5BCS, respectively. Based on these data, the band-gap energy (Eg) of Bi_2S_3 and g-C_3N_4 were calculated using the Tauc/David-Mott model described by the following formula[40].

$$\alpha hv = A(hv - E_g)^{n/2} \quad ...(3)$$

where α was the absorption coefficient and E_g was energy band gap of the samples, h, v and A were the planck constant, optical frequency and constant, respectively. The value of n depended on the

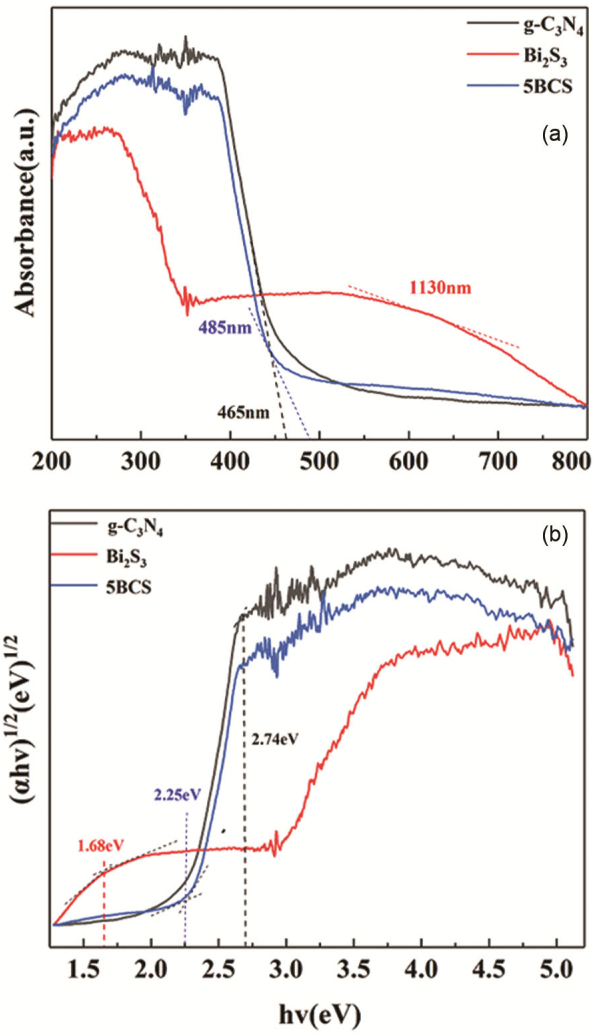

Fig. 4 — (a) UV-vis diffuse reflectance spectra and (b) Plots of $(\alpha hv)^{1/2}(eV)^{1/2}$vs. hv of pure g-$C_3N_4$, bare$Bi_2S_3$ and binary 5BCS.

properties of the transition (direct transition: n = 1; indirect transition: n = 4)[41,42]. g-C_3N_4 belonged to indirect band gap semiconductors and Bi_2S_3 belonged to direct band gap semiconductors, so the n values of the two semiconductors were 4 and 1, respectively. The E_g values were estimated by extrapolation of the linear part of the curves obtained by plotting $(\alpha hv)^{1/2}$ versus hv. As shown in Fig. 4(b), the band gap of g-C_3N_4 was 2.74 eV, which was similar to the results of previous reports[43]. While the band gap of $Bi_2S_3$was 1.68 eV[44]. The band gap had a blue shift relative to the block Bi_2S_3 band gap (1.30eV)[45]. Combining with the size change of Bi_2S_3 nanocrystals, thus it was mainly due to the quantum size effect. Well, the band gap of 5BCS was 2.25 eV, which suggested that the Bi_2S_3 in the composites could markedly lower band

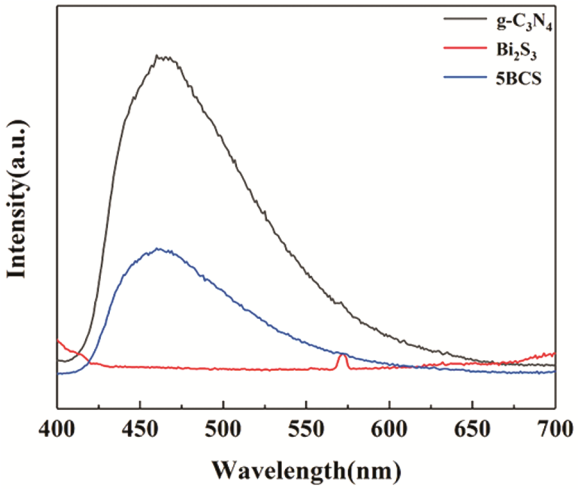

Fig. 5 — PL spectra under the excitation wavelength of 380 nm of pure g-C_3N_4, bareBi_2S_3 and binary 5BCS.

gap of the 5BCS sample. The result reduced the barrier height to be overcome in the transfer of internal electrons, accelerated the electron transfer inside the catalyst, and prolonged the lifetime of electron-hole pairs, which improved photocatalytic activity. Based on the following equation, the potentials of conduction band (CB) and valence band (VB) for a semiconductor material could be calculated according to Eq. (4) and (5):

$$E_{CB} = X - E^e - 0.5E_g \quad \ldots(4)$$

$$E_{VB} = E_{CB} + E_g \quad \ldots(5)$$

where X was the electronegativity of the semiconductor, which was the geometric mean of the electronegativity of the constituent atoms. The X values for g-C_3N_4 and Bi_2S_3 were 4.67 eV and 5.56 eV, respectively[46,47]. E^e was the energy of free electrons on the hydrogen scale (4.5 eV/NHE). Then the E_{VB} of g-C_3N_4 and Bi_2S_3 were calculated to be +1.54 eV and +1.90 eV, the E_{CB} of g-C_3N_4 and Bi_2S_3 were worked out to be -1.20 eV and 0.22 eV, respectively.

PL analysis

The PL spectra were an excellent technique to study the transfer and recombination process of photogenic carriers. As shown in Fig. 5, lower PL intensity represents fast separation and transfer of pairs, thereby leading to a higher degradation rate[48]. It could be seen from the figure that the spectra of g-C_3N_4 showed strong emission peaks at 460 nm,which originated from its rapid charge recombination. The

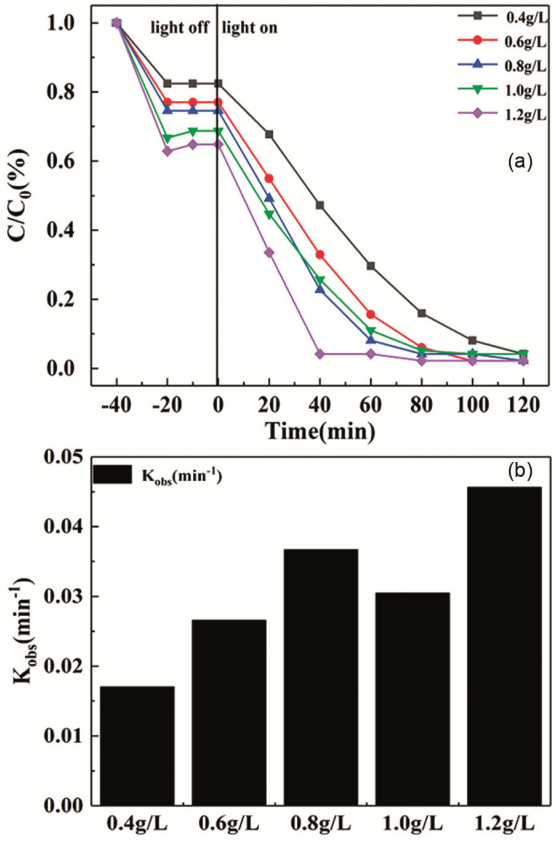

Fig. 6 — (a) Photodegradation and (b) Photocatalytic evaluation for RB19 over the different dosage of 5BCS (C_{RB19}=20mg/L).

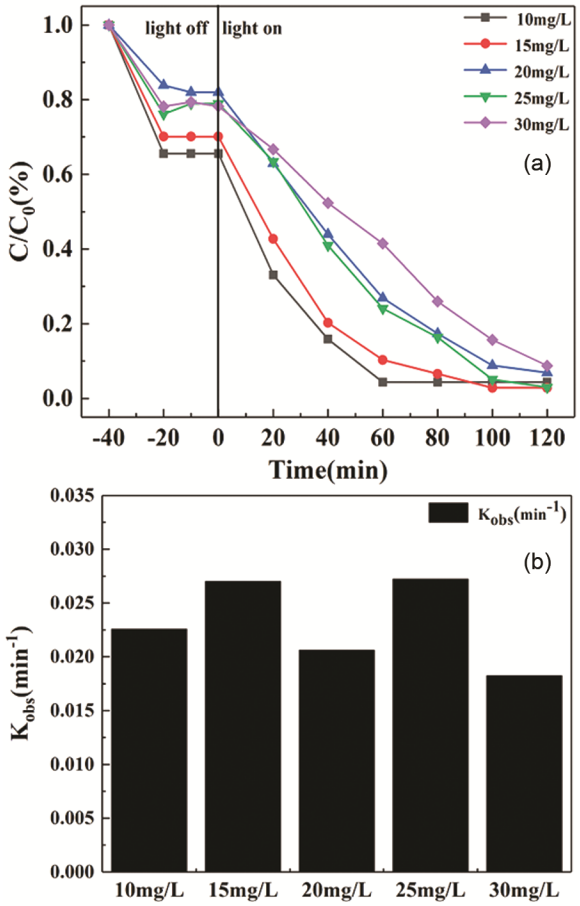

Fig. 7 — (a) Photodegradation and (b) degradation rate constant of RB19 on 5BCS with different concentration (the dosage of catalyst=0.8 g/L).

intensity of the emission peak of Bi_2S_3 at the same location was almost zero, which indicated that Bi_2S_3 had a very low electron-hole recombination rate. The PL spectra of 5BCS at the same location was significantly lower than that of the monomer g-C_3N_4, which displayed that the photogenerated electron-hole pairs of the composite catalysts were effectively separated. As shown above, the recombination rate was reduced and the electron-hole pairs had a longer life. These results proved that the introduction of g-C_3N_4 greatly inhibited the charge carrier. It indicated that the separation efficiency of photogenerated electrons and holes in 5BCS composite catalyst was higher than that of pure g-C_3N_4[49]. The results decreased the recombination of e^--h^+pairs effectively and extended charge carriers lifetime[50].

Photocatalytic activity

Effect of catalyst dosage on the decolorization of RB19

Figure 6(a) displayed the effect of 5BCS dosage on photocatalytic degradation of 20 mg/L RB19. When choosing dosage 0.4, 0.6, 0.8, 1.0 and 1.2 g/L, It could be seen from the diagram that with the increase of the dosage of 5BCS, the dark adsorption of RB19 increased. When the dosages of 5BCS being 0.4, 0.6, 0.8, 1.0 and 1.2 g/L, the dark adsorption rate of the catalyst are 17.60, 23.04, 25.42, 31.29 and 35.20%, respectively. The final degradation efficiency of RB19 were 95.81, 97.81, 97.77, 95.81 and 97.77%. The reason might be deduced: with the increase of photocatalytic dosage, the density of active sites increased. As well as the number of free radical increased, the degradation efficiency improved. When the catalyst load was higher, it will make the solution turbidity increases. It affected the transmission of visible light, so as to reduce the photocatalytic degradation rate[51]. Meanwhile, the K_{obs} degradation of RB19 obviously is displayed in Fig. 6(b). When the dosages of 5BCS were 0.4, 0.6, 0.8, 1.0 and 1.2 g/L, K_{obs} were 1.71×10^{-2}, 2.66×10^{-2}, 3.67×10^{-2}, 3.05×10^{-2} and 4.56×10^{-2} min^{-1}, respectively. According to the dark adsorption capacity, final degradation capacity and degradation rate, the best catalyst dosage was 0.8 g/L.

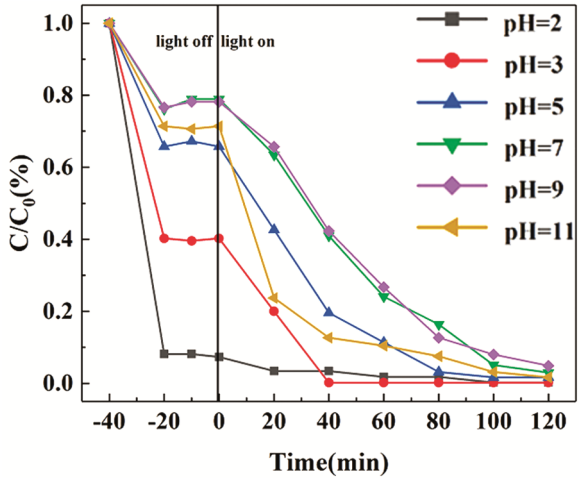

Fig. 8 — Photodegradation of 25 mg/L RB19 on 5BCS with different initial *p*H.

Effect of initial concentration on the decolorization of RB19

In Fig. 7(a), under the optimum value, investigated different initial concentrations of RB19 on photocatalysis. When the initial concentration of RB19 increased from 10 to 30 mg/L, the dark adsorption rate of 5BCS decreased from 30.60% to 18.05% and then increased from 18.05% to 21.80%. It might be inferred: when RB19 was adsorbed on the 5BCS surface at a certain concentration, the e^--h^+ pairs on the photocatalyst surface will be consumed. Simultaneously, the recombination of e^--h^+ pairs will be inhibited and the separation of photogenerated e^--h^+ pairs will be promoted. However, turbidity increased with increasing concentration of RB19. The lower transmittance of visible light leaded to the lower separation of e^--h^+ pairs. Finally, the photocatalytic activity of RB19 was reduced[52]. What's more, the K_{obs} degradation of RB19 obviously displayed in Fig. 7(b). When the concentration was 10, 15, 20, 25 and 30 mg/L, the K_{obs} corresponds to 2.257×10^{-2}, 2.700×10^{-2}, 2.060×10^{-2}, 2.722×10^{-2} and 1.823×10^{-2} min^{-1}, respectively. Therefore, 25 mg/L was chosen as the optimum concentration considering the comprehensive concentration degradation and concentration rate constant analysis.

Effect of initial *p*H on the decolorization of RB19

Figure 8 shows the photodegradation efficiency of different pH solutions. Under the conditions of 0.8 g/L photocatalyst dosage and 25 mg/L initial concentration of RB19 solution, the photocatalytic degradation efficiency of 5BCS was tested by HCl and NaOH adjusting the solution *p*H to 2, 3, 5, 7, 9 and 11. It could be clearly seen that different *p*H

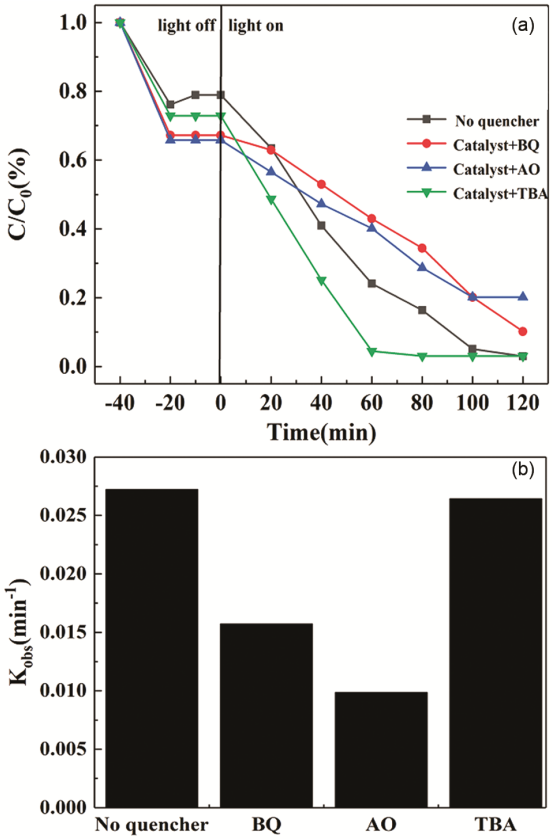

Fig. 9 — (a) Photodegradation and (b) degradation rate constant of 25 mg/L RB19 with different radical scavengers.

affect the dark adsorption capacity of the catalyst. The stronger the acidity, the greater is the dark adsorption capacity, and smallest adsorption capacity in the neutral environment. The dark adsorption capacity were 92.65, 59.75, 34.26, 21.08, 21.83 and 28.62%, respectively, while the final degradation rate was about 95%. This might be determined by the electrochemical characteristics of the catalyst surface and the zero point charge. In neutral environment, RB19 had -SO_3H group and negative charge. Under the conditions of acidic, a large number of positive charges were generated on the surface of the catalyst and reacted with RB19. When in alkaline conditions, a group of negative charges will be rejected by RB19, which inhibited the photocatalytic degradation efficiency[53,54].

Photocatalytic mechanism

In order to ascertain the active species in the degradation process, some sacrificial agents, such as tert-butyl alcohol (TBA), ammonium oxalate (AO) and 1,4-benzoquinone (BQ) were used as the hydroxyl radical (·OH) scavenger, hole (h^+) scavenger

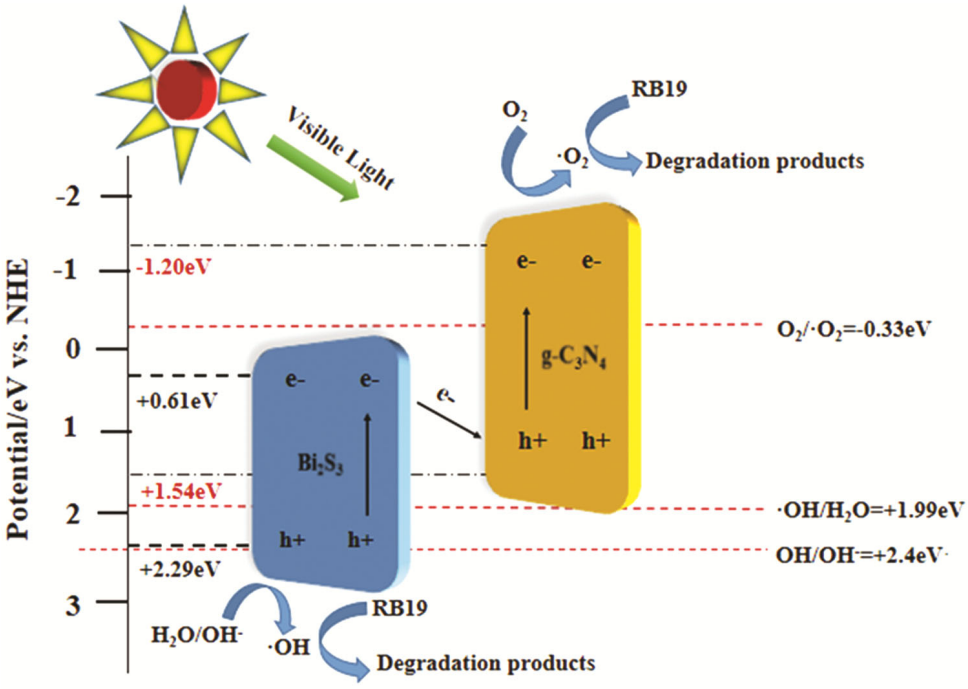

Fig. 10 — Degradation mechanism of RB19 over the 5BCS.

and superoxide radical (O_2^-) scavenger, respectively. The radical-trapping photocatalytic experimental results were presented in Fig. 9(a). It could be seen from the figure that by adding AO of 0.05 mM to remove holes (h^+), the final result of photocatalytic degradation of RB19 by 5BCS was reduced from 96.99 to 79.84%. Then, when BQ of 0.05 mM was added to remove superoxide radical (O_2^-), the photocatalytic degradation efficiency of RB19 changes suddenly dropped from 96.99 to 89.82%, and the photodegradation rate decreased significantly. Finally, TBA of 0.2 mL was added, the degradation efficiency greatly decreased from 96.99% to 96.95%, indicating the ·OH did not play a major role in photocatalytic degradation.It could be seen the effect of scavengers on the photodegradation rate constant in Fig. 9(b), the K_{obs} of 5BCS photocatalytic degradation of RB19 was 2.72×10^{-2} min^{-1}. The K_{obs} of photocatalytic degradation of RB19 by 5BCS were 1.57×10^{-2}, 0.986×10^{-2} and 2.64×10^{-2} min^{-1} with the addition of BQ, AO and TBA. Based on the above experimental results, the above results indicated that the $\cdot O_2^-$ and h^+ radicals were the major active species in the photocatalytic process of RB19 by the system consisted of 5BCS.

Based on the above optical characterization, calculated energy band positions and the active species trapping experiments, a schematic diagram of the band positions of the 5BCS composite and photogenerated charges transfer process were presented in Fig. 10. The possible photocatalytic mechanism was proposed as follows: g-C_3N_4 and Bi_2S_3 were stimulated under light because the energy of light radiation was higher than that of the catalyst itself. Photogenerated electrons (e^-) generated on the conduction band (CB) migrated to the valence band (VB) and left photogenerated holes (h^+) on VB. The results showed that the band gap of g-C_3N_4 was 2.74 eV (vs NHE), CB was -1.2 eV and VB was 1.54 eV, the band gap of Bi_2S_3 was 1.68 eV (vs NHE), CB was 0.61 eV and VB was 2.29 eV. Because the CB potential (-1.2 eV/NHE) of g-C_3N_4 was more negative than that of $O_2/\cdot O_2^-$(-0.33 eV/NHE). A large number of e^- bounded H_2O forms$\cdot O_2^-$ to degrade RB19[55]. Secondly, the VB potential of g-C_3N_4 (-1.54 eV/NHE) was much lower than that required for the formation of OH^- (·OH/ H_2O =+1.99 eV Vs NHE, ·OH /OH^- =+2.4 eV vs NHE), so h^+ on VB could not combine with OH^- to form ·OH. The VB potential of Bi_2S_3 was higher than that of ·OH, so h^+ on VB combined with H_2O and OH^- to form ·OH. However, due to the small amount of Bi_2S_3 doping, the role of ·OH in photocatalysis could be neglected. At the same time, e^- transferring from CB of Bi_2S_3 to h^+ transferring from VB of g-C_3N_4 was due to the shorter distance and less energy consumption compared with VB of Bi_2S_3. The

accumulated h^+ on VB of Bi_2S_3 could directly oxidize and degrade RB19. From the conclusion of trap experiment, a Z-scheme transport mechanism was described between g-C_3N_4 and Bi_2S_3, instead of the traditional heterojunction. All these processes could be described by the follow Eq. (6)-(13):

$$Bi_2S_3 \xrightarrow{hv} Bi_2S_3(e_{CB}^- + h_{VB}^+) \quad \ldots(6)$$

$$g\text{-}C_3N_4 \xrightarrow{hv} g\text{-}C_3N_4(e_{CB}^- + h_{VB}^+) \quad \ldots(7)$$

$$e_{CB}^- + O_2 \rightarrow \cdot O_2^- \quad \ldots(8)$$

$$\cdot O_2^- + RB19 \rightarrow \text{oridation products} \quad \ldots(9)$$

$$h_{VB}^+ + RB19 \rightarrow \text{oridation products} \quad \ldots(10)$$

$$h_{VB}^+ + OH^- \rightarrow \cdot OH \quad \ldots(11)$$

$$h_{VB}^+ + H_2O \rightarrow \cdot OH + H^+ \quad \ldots(12)$$

$$\cdot OH + RB19 \rightarrow \text{oxidation products} \quad \ldots(13)$$

Conclusion

In conclusion, a Z-scheme heterojunction of 5BCS photocatalyst was prepared via a wet impregnation-calcination method for Bi_2S_3 nano ribbons loading on the bare g-C_3N_4. The combination of Bi_2S_3 with optimum weight percentage (5wt%) into g-C_3N_4 significantly increased the photocatalytic RB19 degradation performance, which about 95%. The trapping experiments confirmed that $\cdot O_2^-$ and h^+ were the active species in degrading RB19 with the 5BCS system. In short, the electron transfer increased the lifetime of the electron-hole pairs of the catalyst, thereby improving the photocatalytic performance of the catalyst. The paper provided a new Z-scheme heterojunction of 5BCS and efficient heterogeneous catalyst, which benefited the practical application in treating organic pollutants in waste water.

Acknowledgements

This work was supported by the Natural Science Foundation of Shanxi Province (201901D111068)and Key Research and Development (R&D) Projects of Shanxi Province (201803D31152).

References

1 Samsudin M F R, Bashiri R & Mohammed N M, *Malay J Micro*, 16(2020) 180.
2 Cao S, Low J, Yu J & Jaroniec M, *Adv Mater*, 27(2015) 2150.
3 Huitle C A M & Brillas E, *Appl Catal B: Environ*, 87 (2015) 603.
4 Jing Y J & Kang L, *Ceram Int*, 46 (2020) 18826.
5 Lam S M, Sin J C & Mohamed A R, *Mat Sci Semicon Proc*, 47(2017) 72.
6 Wu M, Lv H, Wang T, Ao Z, Sun H, Wang C, An T& Wang S, *Catal Today*, 315 (2018) 205.
7 Guo J, Lee J, Wang W, Yan X, Gao J & Wang Y, *Catal Comm*, 100 (2017) 223.
8 Zhu W, Sun F, Goei R & Zhou Y, *Catal Sci Technol*, 7(2017) 2591.
9 Fujishima A & Honda K, *Nature*, 238 (1972) 37.
10 Wang R, Hashimoto K & Fujishima A, *Nature*, 388 (1997) 431.
11 Liu M, Jia L, Zhao Z, Han Y, Li Y, Peng Q & Zhang Q, *Chem Eng J*, 390 (2020) 124667.
12 Qiao X, Zhao C, Shao Q & Hassan M, *Energy Fuels*, 32(2018) 6022.
13 Wong J C S, Linsebigler A, Lu G Q, Fan J F & Yates J T J, *J Phys Chem*, 99 (1995) 335.
14 Che H, Liu L, Che G, Dong H, Liu C & Li C, *Chem Eng J*, 357(2019) 209.
15 Xue W, Huang D, Li J, Zeng G, Dong R, Yang Y, Chen S, Li Z, Gong X & Li B, *Chem Eng J*, 373 (2019) 1144.
16 Wang Y X, Rao L, Wang P F, Shi Z Y & Zhang L X, *Appl Catal B: Environ*, 262(2020) 118308.
17 Hu C, Han Q, Zhao F, Yuan Z, Chen N & Qu L, Sci China Mater, 58 (2015) 21.
18 Desipio M M, Bramer S E V, Thorpe R & Saha D, J Hazard Mater, 376(2019) 178.
19 Li Z, Jin C, Wang M, Kang J, Wu Z, Wu D & Zhu T, *Sep Purif Technol*, 232 (2020) 115937.
20 Liu H, Ma S, Shao L, Liu H, Gao Q, Li B, Fu H, Fu S, Ye H, Zhao F&Zhou J, *Appl Catal B: Environ*, 261 (2020) 118201.
21 Pawar, RC, Kang S, Park JH, Kim J, Ahn S&Lee CS, Sci Rep, 6(2016) 31147.
22 Akhundi A&Habibi-Yangjeh A, *J Colloid Interf Sci*, 482 (2016) 165.
23 Jo WK, Kumar S, Eslava S&Tonda S, *Appl Cataly B: Environ*, 239 (2018) 586.
24 Zhang B, Shi H X, Yan Y J, Liu C Q, Hu X Y, Liu E Z & Fan J, *Colloids Surf A*, 608 (2021)125598.
25 Arumugam J, Raj AD, Irudayaraj A A & Thambidurai M, *Mater Lett*, 220 (2018) 28.
26 Guo R, Liu X, Qin H, Wang Z, Xu X, Pan W, Fu Z, Tang J, Jia P, Miao Y & Gu J, *Appl Surf Sci*, 500 (2020) 144059.
27 Mi Y, Li H, Zhang Y, Zhang R & Hou W, *Appl Surf Sci*, 423(2017) 126568.
28 Pirhashemi M & Habibi-Yangjeh A, *Appl Surf Sci*, 283 (2013) 1080.
29 Cao S, Low J, Yu J & Jaroniec M, Adv Mater, 27(2015) 2150.
30 Xiong D, Huang G, Zhou B, Chang S, Wang F & Huang W, *J Phys D Appl Phys*, 30 (2016) 305105.
31 Zhou X, Yao S, Long Y, Wang Z & Li W, *Mater Lett*, 145(2015) 2365.

32 Thongtem T, Phuruangrat A, Wannapop S & Thongtem S, *Mater Lett*, 64 (2010) 122.
33 Chen D, Fang J, Lu S, Zhou G, Feng W, Yang F, Chen Y & Fang Z, *Appl Surf Sci*, 426 (2017) 427.
34 Xu M, Han L & Dong S, *Acs Appl Mater Inter*, 5 (2013) 12533.
35 Wan J, Du X, Liu E, Hu Y, Fan J & Hu X, *J Catal*, 345 (2017) 281.
36 Qu J, Chen D, Li N, Xu Q, Li H, He J & Lu J, *Appl Catal B Environ*, 207 (2017) 404.
37 Ke J, Liu J, Sun H, Zhang H, Duan X, Liang P, Li X, Tade M, Liu S & Wang S, *Appl Catal B Environ*, 200 (2017) 47.
38 Wu Z, Chen L, Xing C, Dong J, Jiang X&Chen M, *Dalton Trans*, 42 (2013) 12980.
39 Dai X, Xie M, Meng S, Fu X & Chen S, *Appl Catal B Environ*, 158(2014) 382.
40 Shiraishi Y, Kofuji Y, Sakamoto H, Tanaka S, Ichikawa S & Hirai T, *Acs Catal*, 5 (2015) 3058.
41 Long Y, Wang Y, Shen H, Zhang Y, Li J & Wang D, *Appl Surf Sci*, 393(2017) 496.
42 Yousefi M, Sabet M & Salavati-Niasari M, *J Clust Sci*, 23 (2012) 511.
43 Kumar S, Tonda S, Baruah A, Kumar B & Shanker V, *Dalton Trans*, 42 (2014) 16105.
44 Teng QQ, Upmann D, Wijaya SAZN & Huynh V, *Organometallics*, 13 (2016) 3373.
45 Talhaoui N, Gómez-Caravaca AM, León L, Rosa RDI, Fernandez-Gutierrez A & Segura-Carretero A, *Int J Mol Sci*, 17(2016) 337.
46 Yun HN, Ikeda S, Matsumura M & Amal R, *Energy Environ Sci*, 5(2012) 9307.
47 Jo W K & Selvam N C S, *Chem Eng J*, 317 (2017) 913.
48 Zhou X, Shao C, Li X, Wang X, Guo X & Liu Y, *J Hazard Mater*, 344 (2017) 113.
49 Shi H, Zhao Y, Fan J & Tang Z, *Appl Surf Sci*, 465 (2019) 212.
50 Zhu C, Gong T, Xian Q & Xie J, *Appl Surf Sci*, 444 (2018) 75.
51 Vaiano V, Matarangolo M & Murcia J J, *Appl Catal B Environ*, 225 (2018) 197.
52 Wu Y, Wang H, Tu W, Liu Y, Tan Y, Yuan X & Chew J, *J Hazard Mater*, 347(2018) 412.
53 Kalikeri S, Kamath N, Gadgil D J & Kodialbail VS, *Environ Sci Pollut R*, 25 (2018) 3731.
54 Shao B, Liu X, Liu Z, Zeng G, Liang Q, Liang C, Cheng Y, Zhang W, Liu Y & Gong S, *Chem Eng J*, 368 (2019) 730.
55 Chen D, Fang J, Lu S, Zhou G, Feng W, Yang F, Chen Y & Fang Z, *Appl Surf Sci*, 426 (2017) 427.